Arabian Journal of Chemistry (2022) **15**, 104347

King Saud University

Arabian Journal of Chemistry

www.ksu.edu.sa
www.sciencedirect.com

ORIGINAL ARTICLE

Exploring high pressure structural transformations, electronic properties and superconducting properties of MH_2 (M = Nb, Ta)

Jinquan Zhang [a], Yanqi Wang [a], Libiao Tang [a], Juyi Duan [a], Jingjing Wang [b], Song Li [a], Meng Ju [c], Weiguo Sun [d], Yuanyuan Jin [a,*], Chuanzhao Zhang [a,*]

[a] *Department of Physics and Optoelectronic Engineering, Yangtze University, Jingzhou 434023, China*
[b] *College of Computer and Information Engineering, Hubei Normal University, Huangshi 435002, China*
[c] *School of Physical Science and Technology, Southwest University, Chongqing 400715, China*
[d] *College of Physics and Electronic Information, Luoyang Normal University, Luoyang 471022, China*

Received 4 August 2022; accepted 9 October 2022
Available online 18 October 2022

KEYWORDS

Metal hydrides;
First-principles calculation;
High pressure;
Electron localization function;
Superconductivity;
Pressure–temperature phase diagram

Abstract The high-pressure structures and properties of MH_2 (M = Nb, Ta) are explored through an ab initio evolutionary algorithm for crystal structure prediction and first-principles calculations. It is found that NbH_2 undergoes a phase transition from a cubic *Fm*3*m* structure with regular NbH_8 cubes to an orthorhombic *Pnma* structure with fascinating distorted NbH_9 tetrakaidecahedrons at 48.8 GPa, while the phase transition pressure of TaH_2 from a hexagonal $P6_3mc$ phase with slightly distorted TaH_7 decahedron to an orthorhombic *Pnma* phase with attractive distorted TaH_9 tetrakaidecahedrons is about 90.0 GPa. Besides, the calculated electronic band structure and density of states demonstrate that all of these structures are metallic. The Poisson's ratio, electron localization function, and Bader charge analysis suggest that these phases possess dominant ionic bonding character with the effective charges transferring from the metal atom to H. From our electron–phonon calculations, the calculated superconducting critical temperature T_c of the *Pnma*-NbH_2 is 6.903 K at 50 GPa. Finally, via the quasi-harmonic approximation method, the phase diagrams at pressure up to 300 GPa and temperature up to 1000 K of MH_2 (M = Nb, Ta) are established, where the transition pressure of *Fm*3*m*-NbH_2 → *Pnma*-NbH_2 and $P6_3mc$-TaH_2 → *Pnma*-TaH_2 were found to decrease with increasing temperature.

* Corresponding authors.
E-mail addresses: scujyy@163.com (Y. Jin), zcz19870517@163.com, jyy@163.com (C. Zhang).
Peer review under responsibility of King Saud University.

Production and hosting by Elsevier

https://doi.org/10.1016/j.arabjc.2022.104347

1. Introduction

Metal hydrides, especially under high pressure, have attracted wide attention because of their unique physical properties and attractive applications, such as potential high-temperature superconductivity and clean energy with the ability to replace fossil fuels as hydrogen storage materials. For example, some hydrogen-rich compounds, including YH_6 (Troyan et al., 2021; Kong et al., 2021), YH_9 (Snider et al., 2021), CeH_9 (Salke et al., 2019; Li et al., 2019), CeH_{10} (Chen et al., 2021), ThH_9 (Semenok et al., 2020), ThH_{10} (Semenok et al., 2020), LaH_{10} (Drozdov et al., 2019), SnH_{12} (Hong et al., 2021; Talantsev, 2021); UH_7 (Kruglov et al., 2018); and CaH_6 (Ma et al., 2022; Li et al., 2022), have been proved to have good superconductivity with high superconducting temperatures ranging from 44 to 262 K at high pressures and a hydrogen-rich compound rhodium trihydride (RhH_3) with a high volumetric hydrogen density of 212.5 g H_2/L could be used as a hydrogen storage material (Shao et al., 2021).

In recent years, transition metal hydrides have also been extensively studied under high pressure, which can be summarized as the following two aspects. On the one hand, the late transition metals with higher and comparable electronegativity values (e.g., 2.2 for Ru, Pd, Os, and Ir; 2.28 for Pt; 2.36 for W; 2.54 for Au) than that of hydrogen (2.2) are unfavorable react with hydrogen at ambient pressure. However, fortunately, high pressure can make the chemical potential of hydrogen rise sharply, thus effectively stimulating the chemical reactivity of elements, which makes the reaction between hydrogen and post-transition metals become a reality (Miao et al., 2020). Previous high-pressure experiments have shown that high pressure makes it possible to synthesize Rh, Ir, and Pt hydrides. For example, a potential hydrogen source material rhodium dihydride RhH_2 (Li et al., 2011) with a volume hydrogen density of 163.7 g H_2/L was discovered at room temperature at 8 GPa, and iridium trihydride IrH_3 (Scheler et al., 2013) was successfully synthesized above 65 GPa at room temperature by in-situ X-ray diffraction measurement. Besides, PtH is a superconductor with T_c = 10–25 K at high pressure (Kim et al., 2011). On the other hand, as for the early transition metals, although it is found that they are easy to form hydrides under environmental conditions, such as ScH_2/ScH_3, YH_2/YH_3, TiH_2, ZrH_2, HfH_2, VH_2, and NbH_2, after compression, some transition metal hydrides show attractive characteristics and undergo complex phase transitions that cannot be found under normal conditions (Miwa and Fukumoto, 2002; Quijano et al., 2009; Kanagaprabha et al., 2013; Smithson et al., 2002; Purans et al., 2021). For example, theoretical studies show that TiH_2 undergoes a structural transition of $I4/mmm \rightarrow P4/nmm \rightarrow P2_1/m$ under high pressure at the corresponding transition pressures of 63 GPa and 294 GPa, respectively, and the phase transition from $I4/mmm$ to $P4/nmm$ at 63 GPa is more suitable for the experimental XRD pattern and the resulting unit cell parameters (Gao et al., 2013; Kalita et al., 2010). A subsequent experiment on the structures and properties of ZrH_2 were also investigated under high pressure, which provided a new method for finding hydrogen structures with higher bulk density in transition metal hydrides without static pressure or shear stress (Huang et al., 2014). Subsequently, the theoretical study of HfH_2 revealed that it undergoes pressure-induced structural phase transition $I4/mmm \rightarrow Cmma \rightarrow P2_1/m$ at 180 GPa and 250 GPa, respectively, and the T_c of $P2_1/m$-HfH_2 at 260 GPa is 10.62–12.8 K (Liu et al., 2015). Moreover, Ye *et al.* reported that the structural sequence of ScH_2 should be $Fm\bar{3}m \rightarrow C2/m$, with transformation pressures of 65 GPa (Ye et al., 2015). Recent ab initio calculations predicted that $Fm\bar{3}m$-ScH_2 (Wei et al., 2016) with T_c up to 38.11 K at 30 GPa is close to that of MgB_2 (39 K) (Choi et al., 2002; Bohnen et al., 2001). This motivated us to find its new structures and explore the high-temperature superconductive property by compressing compounds of early transition metals with hydrogen.

With regard to group 5 element dihydrides, the high-pressure structures and related structural and electronic properties of VH_2 and NbH_2 have also been deeply explored under high pressure. The two groups predicted that VH_2 transforms from cubic $Fm\bar{3}m$ structure to orthogonal $Pnma$ phase at about 50 GPa and the T_c estimate of two stable VH_2 structures is only several Kelvins (Chen et al., 2014; Wang et al., 2020). As for NbH_2, Gao *et al.* report a phase transition sequence of $Fm\bar{3}m \rightarrow Pnma$ at 50 GPa (Gao et al., 2013; Liu et al., 2017). However, Chen *et al.* used an evolutionary algorithm to detect their stability in the pressure range of 0–100 GPa and found that the ground state $Fm\bar{3}m$-NbH_2 transformed to $P6_3mc$-NbH_2 at about 43 GPa (Chen et al., 2014). However, the obtained phase transition sequences of NbH_2 were not in agreement with each other. In recent experiments, the tantalum dihydride phase was synthesized at about 5 GPa. Despite large amounts of experimental research on TaH_2 (Saitoh et al., 2021; Kuzovnikov et al., 2017; Ying et al., 2019; Kuzovnikov et al., 2020), there are few theoretical studies on the high-pressure phase transition of TaH_2 and its mechanical properties, chemical bonding nature, dynamical properties, and superconductivity under high pressures. Therefore, this stimulates us to explore of high-pressure structures of MH_2 (M = Nb, Ta) and completely understand the structural characters, mechanical properties, electronic properties, and superconductivity of both dihydrides.

In this paper, we examine in detail the crystal structures of MH_2 (M = Nb, Ta) within the pressure range of 0–300 GPa by employing an ab initio evolutionary algorithm in combination with first-principles calculations. Interestingly, our calculated results show that NbH_2 and TaH_2 adopt the $Fm\bar{3}m$ and $P6_3mc$ structure, respectively, at low pressures. However, at high pressures, NbH_2 and TaH_2 possess the same $Pnma$ phases. Band structures and density of states indicate that these structures are metallic, while the estimated T_c is 0.945–1.836 K for $Fm\bar{3}m$-NbH_2 at 1 atm, 0.775–1.528 K for $P6_3mc$-TaH_2 at 1 atm, 4.485–6.795 K for $Pnma$-NbH_2 at 100 GPa, and 3.586–5.542 K for $Pnma$-TaH_2 at 100 GPa, respectively. In addition, the analyses of the Poisson's ratio, electron localization function (ELF), and Bader charge show that these phases are ionic crystals with the charges transferring from the metal atom to H. Furthermore, the calculation results of the pressure–temperature phase diagram of MH_2 (M = Nb, Ta) based on the quasi-harmonic approximation method indicate that high temperature and low pressure are more favorable to synthesizing the high-pressure phase of MH_2 (M = Nb, Ta). Our present research attempts to better understand the behavior and properties of MH_2 (M = Nb, Ta) under pressure and temperature, and promote further experimental and theoretical research on transition metal hydrides.

2. Computational method

We use the evolutionary algorithm USPEX code (Universal Structure Predictor: Evolutionary Xtallograph) to predict crystal structure, so as to extensively explore stable low-energy structures under high pressure with a different number of formula units (f.u.) at zero temperature (Oganov and Glass, 2006; Oganov et al., 2011; Lyakhov et al., 2013). A similar method has been successfully applied to discover transition metal dichalcogenides under high pressure with a similar composition to MH_2 (M = Nb, Ta) and provides good guidance for the synthesis of experiments (Saqib et al., 2021; Rahman et al., 2022). Here, we have predicted the crystal structure of MH_2 (M = Nb, Ta) at 1 atm, 50, 100, 150, 200, 250, and 300 GPa, in which the unit cell is as high as 8 formula units. The 50 structures of the first generation are randomly generated by the evolutionary algorithm, 60 % of the structures of each subsequent generation come from the parent generation, and the new structures of each subsequent generation are generated by mutation operator inheritance (60 %), substitution (10 %) and lattice mutation (30 %). The energy calcu-

lations, electronic structure calculations, and elastic properties introduced in this paper are carried out in density functional theory within the Perdew-Burke-Ernzerhof (PBE) parameterization of the generalized gradient approximation (GGA) as implemented in the Vienna ab initio simulation software package (VASP) (Kresse and Furthmüller, 1996; Perdew et al., 1996). The Projector-Augmented Wave (PAW) potentials with 13 valence electrons ($4s^2 4p^6 5s^1 4d^4$) for Nb, 11 valence electrons ($5p^6 6s^2 5d^3$) for Ta, and 1 valence electron ($1\ s^1$) for H were applied with a plane wave basis set up to cutoff energy of 600 eV and the k-point grid with 0.2 $Å^{-1}$ spacing was used to sample the Brillouin zone to ensure that all enthalpy calculations are well converged to < 1 meV/atom (Kresse and Joubert, 1999; Monkhorst and Pack, 1976). We use Bader charge analysis (Tang et al., 2009) and electronic localization function (Becke and Edgecombe, 1990; Savin et al., 1992) to describe electronic properties. In order to determine the dynamic stability and thermodynamic properties of the studied structure, the phonon calculation is carried out by using the supercell method with PHONOPY program (Togo et al., 2008; Togo and Tanaka, 2015). The independent single crystal elastic constants could be determined by applying a stress tensor generated by a small strain to an optimized unit cell. The bulk modulus (B), shear modulus (G), Young's modulus (E), and Poisson's ratio (ν) of the material were determined by Voigt-Reuss-Hill (VRH) approximation (Hill, 1952). Electron–phonon coupling (EPC) parameter λ of NbH_2 and TaH_2 is performed using the density functional perturbation theory as implemented in the QUANTUM-ESPRESSO package (Giannozzi et al., 2009). The Projector-Augmented Wave (PAW) potentials were applied with a plane wave basis set up to cutoff energy of 60 Ry and charge density cutoff of 600 Ry. The q-point mesh of EPC calculations adopted $6 \times 6 \times 6$ for $Fm\bar{3}m$-NbH_2, $2 \times 4 \times 2$ for $Pnma$-NbH_2, $4 \times 4 \times 2$ for $P6_3mc$-TaH_2, and $2 \times 4 \times 2$ for $Pnma$-TaH_2, respectively.

3. Results and discussion

3.1. Crystal structure searching and phase transition under pressure

Firstly, to extensively explore the stable MH_2 (M = Nb, Ta) under different pressures, we carry out the evolutionary structural search for MH_2 (M = Nb, Ta) using simulation sizes ranging from one to eight MH_2 (M = Nb, Ta) formula units (f.u.) in the unit cell at 0 K with selected pressures of 1 atm, 50, 100, 150, 200, 250, and 300 GPa. Subsequently, the analysis of the predicted structures provides some candidate structures with space groups Pm, $C2/m$, $Pnma$, $Imma$, $P4/nmm$, $P\bar{3}m1$, $P6_3mc$, and $Fm\bar{3}m$ for NbH_2, and Pm, $Pnma$, $P6_3/mmc$, $P4/nmm$, $Fm\bar{3}m$, $P\bar{3}m1$, $P6_3mc$, and $P\bar{6}2m$ for TaH_2. The enthalpy-pressure (H—P) relations of the candidate structures relative to the cubic $Fm\bar{3}m$ phase under the pressure range of 0–300 GPa for NbH_2 and TaH_2 are presented in Fig. 1a and Fig. 1c. According to our simulation, NbH_2 and TaH_2 at

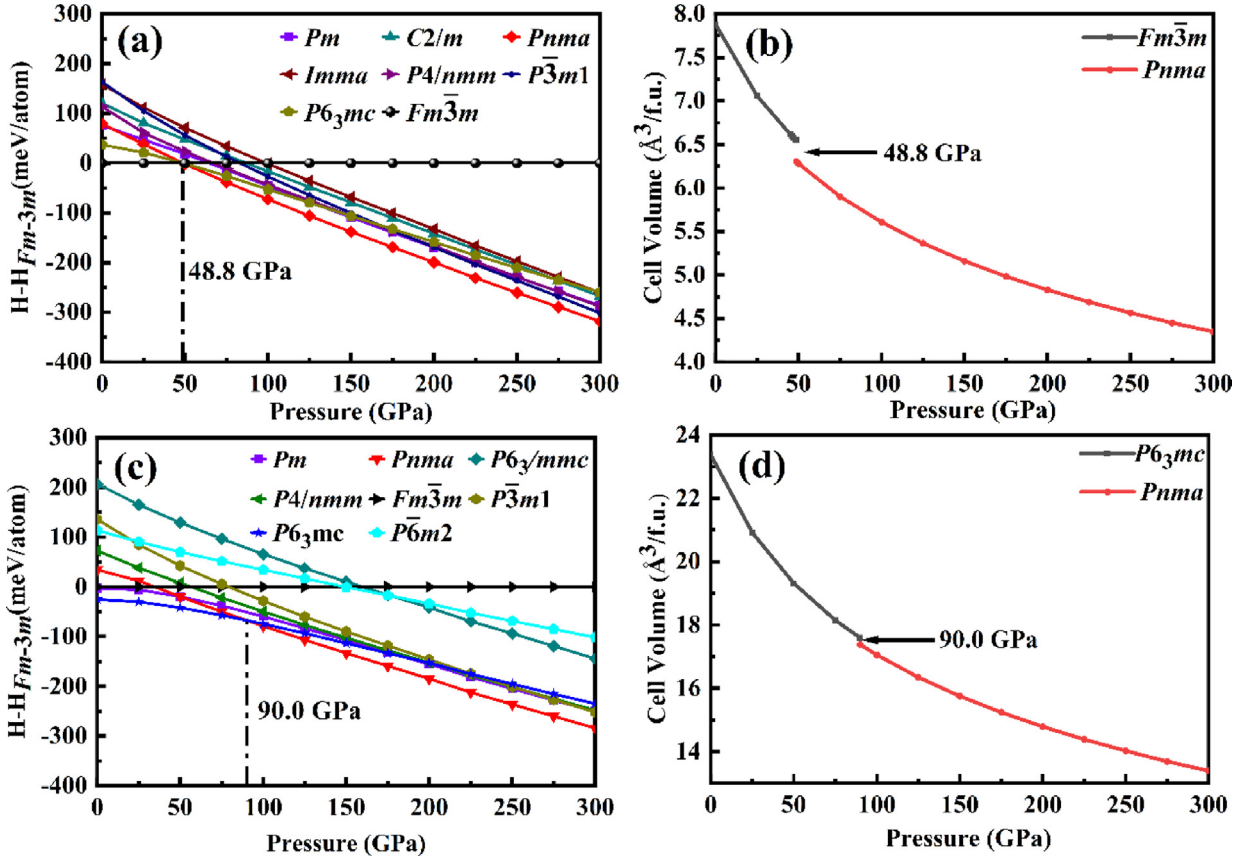

Fig. 1 (a) Enthalpy-pressure relation concerning the $Fm\bar{3}m$ phase and (b) volume-pressure relations for NbH_2. (c) Enthalpy-pressure relation concerning the $Fm\bar{3}m$ phase and (d) volume-pressure relations for TaH_2.

1 atm adopt the structures of $Fm\bar{3}m$ and $P6_3mc$, respectively, which is consistent with the experimental observations (Reilly and Wiswall, 1970; Saitoh et al., 2021; Kuzovnikov et al., 2017; Ying et al., 2019; Kuzovnikov et al., 2020). The fact that all the experimental and theoretical structures are successfully reconstructed in a specific pressure range verifies the rationality of our method. Under compression, we observed the orthorhombic *Pnma* structure is favored over the cubic $Fm\bar{3}m$ phase above 48.8 GPa for NbH_2 and the hexagonal $P6_3mc$ phase above 90.0 GPa for TaH_2, which does not include zero point energy (ZPE). Because of the extremely light mass of hydrogen atoms, it is expected that quantum effects will play an important role, and the (ZPE) of hydrogen may be large enough to affect the structural stability of the calculated phase (Pickard and Needs, 2007). We will discuss the influence of zero point energy on phase stability in Section 3.5. The calculated equations of state (EOS) for ambient-pressure structures and the orthorhombic *Pnma* structures show the volumetric changes are discontinuous at the transition point as plotted in Fig. 1b and Fig. 1d. We observed a volume collapse of 3.7 % occur at 48.8 GPa for NbH_2 and 1.2 % occur at 90.0 GPa for TaH_2, suggesting that the two-phase transitions are the first-order transition.

To further verify the stability of four structures in comparison with other M−H (M = Nb, Ta) compositions, the typical convex hull diagrams of the M−H system are plotted in Fig. S1 at 1 atm, 100 GPa, 200 GPa, and 300 GPa. (Fig. S1 in the Supplementary Material) It is found that MH_2 (M = Nb, Ta) always lie on the convex hull curve, suggesting that they are thermodynamically stable under both high pressure and low pressure. Besides, we approach the pressure dependence of the MH_2 (M = Nb, Ta) decomposition reaction (see Fig. S2). Fig. S2a shows that NbH_2 can't decompose to $NbH + \frac{1}{2}H_2$ or $\frac{1}{3}Nb + \frac{2}{3}NbH_3$. For TaH_2, we consider three substantially different decomposition paths displayed in Fig. S2b: $\frac{1}{2}Ta_2H + \frac{3}{4}H_2$, $TaH + \frac{1}{2}H_2$, or $\frac{1}{3}Ta + \frac{2}{3}TaH_3$. (Fig. S2 in the Supplementary Material) Apparently, TaH_2 can be stabilized in 0–300 GPa. Through the above discussion, we can conclude that MH_2 (M = Nb, Ta) are ground states at 0–300 GPa without phase separation.

3.2. Structural features

The crystal structures of the thermodynamically stable phases at the corresponding pressures are illustrated in Fig. 2 and their structural parameters, together with previous experimental data, are presented in Table 1 and Table S1. (Table S1 in the Supplementary Material) The $Fm\bar{3}m$-NbH_2 phase at 1 atm, shown in Table 1, has lattice parameters of $a = b = c = 4.556$ Å, which is in good agreement with previous experimental results ($a = b = c = 4.53$ Å) with a lattice parameter difference of 0.57 % and other theoretical results (Zhang et al., 2017; Gao et al., 2013; Liu et al., 2017; Saitoh et al., 2021). For $Fm\bar{3}m$-NbH_2 at atmospheric pressure, each Nb atom is surrounded by 8H atoms to form a regular NbH_8 cube with an Nb-H separation of 1.982 Å. For *Pnma* phase at 100 GPa, each Nb atom is surrounded by 9H atoms. The Nb-H distances range from 1.791 Å to 2.077 Å, and the H-Nb-H angle ranges from 57° to 121°, which indicates that the

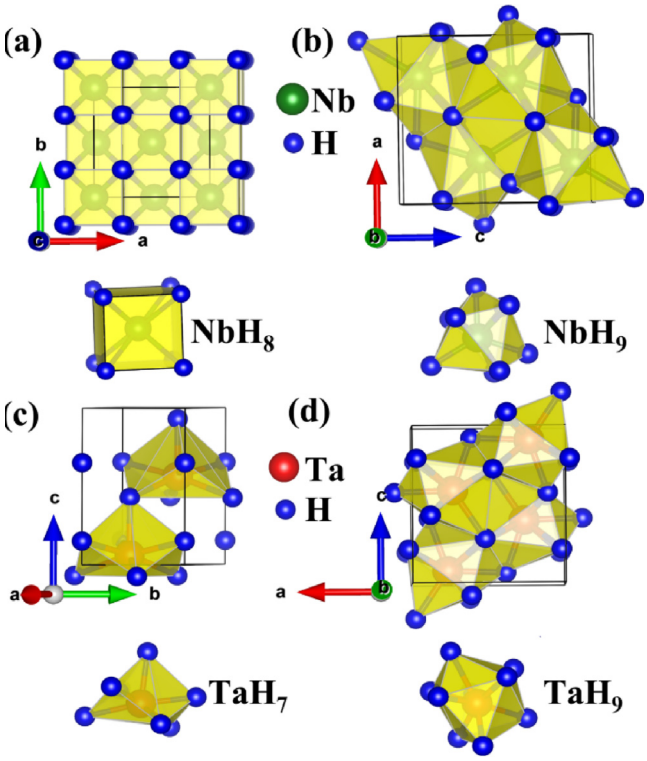

Fig. 2 Crystal Structures of MH_2 (M = Nb, Ta) phases, together with metal coordination polyhedral: (a) $Fm\bar{3}m$-NbH_2 at 1 atm, (b) *Pnma*-NbH_2 at 100 GPa, (c) $P6_3mc$-TaH_2 at 1 atm, and (d) *Pnma*-TaH_2 at 100 GPa. Green atoms depict Nb and red atoms depict Ta, while blue atoms present H.

NbH_9 arrangement in *Pnma* phase is a highly distorted tetrakaidecahedron. Obviously, with the increase of pressure, the Nb-H environment in NbH_2 changes from regular NbH_8 cube to highly distorted NbH_9 tetrakaidecahedron.

For the $P6_3mc$-TaH_2 at ambient pressure, the lattice parameter ($a = b = 3.231$ Å, $c = 5.162$ Å) is in excellent agreement with the previous results ($a = b = 3.222$ Å, $c = 5.153$ Å) calculated by Zhang *et al.* (Zhuang et al., 2017) and experimental data (Kuzovnikov et al., 2020) ($a = b = 3.223$ Å, $c = 5.143$ Å), with a lattice constant deviation of 0.4 %. The third-order Birch-Murnaghan equation of state (EOS (Birch, 1947) is used to determine the bulk modulus B_0, its pressure derivative B_0' and the unit cell volume V_0 at ambient conditions of $P6_3mc$-TaH_2 (see Table 1).

By fitting for $P6_3mc$-TaH_2, the following parameters are obtained: $B_0 = 180$ GPa, $B_0' = 4.08$, and $V_0 = 23.34$ Å^3. These values are in agreement with previous Energy-dispersive X-ray diffraction studies ($B_0 = 210(20)$ GPa, $B_0' = 4$, and $V_0 = 23.14$ Å^3) (Kuzovnikov et al., 2020). As displayed in Fig. 2a, each Ta atom is surrounded by one H atom at a separation of 1.889 Å, three H atoms at a separation of 1.921 Å, and a further three H atoms at a separation of 1.990 Å. In addition, the H-Ta-H angles vary from 68° to 115°. Therefore, the Ta environment in the $P6_3mc$ configuration can be described as distorted TaH_7 decahedrons. In the *Pnma* phase at 100 GPa (see Fig. 2b), the Ta-H distances range from 1.787 to 2.06 Å and the H-Ta-H angles vary from 58° to 164°. These results describe that the Ta environment in the

Table 1 Compound MH_2 (M = Nb, Ta) unit cell lattice parameters, volume, bulk modulus B_0, and its pressure derivative B'_0 at selected pressure.

	Space group	Pressure	Refs	a (Å)	b (Å)	c (Å)	V (Å^3)	B_0	B'_0
NbH_2	$Fm\bar{3}m$	1 atm	This work	4.556				178	3.92
			Experiment (Reilly and Wiswall, 1970)	4.530					
			Calculation (Chen et al., 2014)	4.558					
			Calculation (Zhang et al., 2017)	4.577					
NbH_2	*Pnma*	100 GPa	This work	4.682	2.838	5.067			
			Calculation (Gao et al., 2013)	4.704	2.860	5.085			
			Calculation (Zhang et al., 2017)	4.696	2.862	5.092			
TaH_2	$P6_3mc$	1 atm	This work	3.231	3.231	5.162	23.34	180	4.08
			Calculation (Zhuang et al., 2017)	3.222	3.222	5.153			
			Experiment (Kuzovnikov et al., 2020)	3.223	3.223	5.143	23.14	210(20)	4
TaH_2	*Pnma*	100 GPa	This work	4.709	2.842	5.095	17.04		

Pnma phase is strongly distorted TaH_9 tetrakaidecahedron. In short, the structural features of $P6_3mc$ and *Pnma* TaH_2 can be summarized as slightly distorted TaH_7 decahedrons and strongly distorted TaH_9 tetrakaidecahedron, respectively.

3.3. Mechanical stability, mechanical properties, and electronic properties

To inspect the mechanical stabilities of MH_2 (M = Nb, Ta) structures, we calculated the elastic constants of MH_2 (M = Nb, Ta) at different pressures by using the strain–stress method, as summarized in Table 2. As given in Table 2, four phases satisfy their respectively mechanical stability standards, which state that four structures are mechanically stable at ambient pressure. Besides, Fig. S3 shows that the *Pnma*-NbH_2 and *Pnma*-TaH_2 are dynamically stable at 1 atm, which means that the high-pressure phases *Pnma*-NbH_2 and *Pnma*-TaH_2 can be quenched to normal pressure. (Fig. S3 in the Supplementary Material) At the same time, the bulk modulus (B), shear modulus (G), B/G, Young's modulus (E), and Poisson's ratio (v) can be derived from the calculated elastic constants on the basis of the Voigt-Reuss-Hill method. Firstly, the bulk modulus B of $Fm\bar{3}m$-NbH_2 and $P6_3mc$-TaH_2 is consistent with the zero-pressure bulk modulus B_0 fitted by EOS (see Table 1), which underlines the accuracies of our calculations. The calculated bulk modulus (B), shear modulus (G), and Young's modulus (E) of MH_2 (M = Nb, Ta) at 1 atm are all larger than those of MgH_2 and *Pnma*-TiH_2 hydrogen storage materials, implying that these MH_2 (M = Nb, Ta) dihydrides present good mechanical properties (Junkaew et al., 2014; Pan and Chen, 2020). As we all know, the ductility or brittleness of materials can be estimated by the value of B/G with 1.75 as the critical value (Pugh, 1954). Our results show that the calculated identical ratio values of B/G for $Fm\bar{3}m$-NbH2, *Pnma*-NbH_2, $P6_3mc$-TaH_2, and *Pnma*-TaH_2, are 2.31, 2.07, 2.20, and 2.27, respectively, indicating their toughness behavior. Poisson's ratio is an important parameter to describe the type of bonding in a material (Haines et al., 2001). The threshold value of Poisson's ratio v for covalent, and ionic materials is 0.25: large v values (>0.25) correspond to ionic or metallic materials, while smaller v values (<0.25) correspond to

Table 2 The calculated elastic constants C_{ij} (GPa), bulk modulus B (GPa), shear modulus G (GPa), Young's modulus E (GPa), B/G, Poisson's ratio v, and hardness H_v (GPa) for TaH_2 and NbH_2 at the selected pressures.

Phase	NbH_2		TaH_2		MgH_2 (Junkaew et al., 2014)	TiH_2 (Pan and Chen, 2020)
	$Fm\bar{3}m$	*Pnma*	$P6_3mc$	*Pnma*	$P4_2/mnm$	*Pnma*
Pressure	1 atm	1 atm	1 atm	1 atm	1 atm	1 atm
C_{11}	273	273	312	288	74.4	262.6
C_{22}		242		284		273.3
C_{33}		248	313	263	136.0	248.0
C_{44}	84	77	78	74	37.6	45.1
C_{55}		68		70		83.7
C_{66}		81	73	85	53.0	13.4
C_{12}	133	102	166	140	38.8	55.8
C_{13}		89	95	105	31.4	104.8
C_{23}		121		122		75.6
B	180	154	183	174	54.2	139.5
G	78	75	83	77	37.8	51.5
E	204	193	216	200	92.1	51.5
B/G	2.31	2.07	2.20	2.27		2.71
v	0.31	0.29	0.3	0.31		
H_v	6.6	7.6	7.5	6.6		

covalent materials. The Poisson's ratios of $Fm\bar{3}m$-NbH_2, *Pnma*-NbH_2, $P6_3mc$-TaH_2, and *Pnma*-TaH_2, are all larger than 0.25, suggesting that they can be classified into ionic materials and that the ionic bond component is dominant. Vickers hardness was estimated according to the empirical model proposed by Chen *et al* (Chen et al., 2011). This model is applied as follows: $H_v = 2(K^2G)^{0.585}$-3, where $K = G/B$. The estimated hardness values are 6.6 GPa for $Fm\bar{3}m$-NbH_2, 7.6 GPa for *Pnma*-NbH_2, 7.5 GPa for $P6_3/mc$-TaH_2, and 6.6 GPa for *Pnma*-TaH_2 at 1 atm, which are lower than that of Pd_2Mo_3N with the strong three-dimensional covalent network (17.1 GPa) (Errandonea et al., 2010). Due to strong ionic bonds, the hardness values of all MH_2 (M = Nb, Ta) phases are lower than 10 GPa.

To further gain insight into the electronic properties of four stable MH_2 (M = Nb, Ta) compounds, we calculated the electronic band structures and densities of states (DOS), as displayed in Fig. 3. We can see that they all exhibit metallic characteristics, confirmed by the overlap between the conduction bands and the valence bands, and the finite electronic DOS at the Fermi level (E_f). The metallic behavior of these phases indicates that these materials may be magnetic. We have carried out calculations taking into account the spin polarization. Results suggest that MH_2 (M = Nb, Ta) are all nonmagnetic because the magnetic moment of each mental atom is zero. For these phases, it is found that there is a deep valley below the Fermi level, and the localized hybridization between M-*d* and H-*s* is observed in the energy region below the pseudogap, while the contributions of M-*d* (M = Nb, Ta) states mainly dominate in this energy range above pseudogap, so the metallic properties are mainly due to partially filled Nb-4*d* or Ta-5*d* shell. Note that the contribution from H-*s* states at the Fermi level is almost zero, which is of great significance to superconductivity according to previous studies as will be discussed later.

To clarify the bonding futures for these phases MH_2 (M = Nb, Ta), we calculated the electronic localization function (ELF), as depicted in Fig. 4. It is worthy pointing out that these four crystals display a common feature of the ELF that there is no electron localization toward the neighboring M−H and H—H connections, thus suggesting that no covalent interaction exists for neighboring M−H and H—H. Moreover, the ELF values between M and the nearest H atom in four crystals are all smaller than 0.5, implying that ionic bonds are present between M and H atoms. This conclusion also demonstrates the validity of the analyses of Poisson's ratio. In addition, in order to evaluate the strength of ionic bonds, we explicitly calculated the actual charge transfer between MH_2 (M = Nb, Ta) and H atoms, which is summarized in Table 3. Each H atom respectively gains approximately 0.65 e, 0.51 e, 0.59 e, and 0.52 e for $Fm\bar{3}m$-NbH_2, *Pnma*-NbH_2, $P6_3mc$-TaH_2, and *Pnma*-TaH_2, while the M (M = Nb, Ta) atoms lose approximately 1.30 e, 1.02 e, 1.18 e, and 1.04 e. Therefore, there is a large amount of charge transfer from M (M = Nb, Ta) to the H

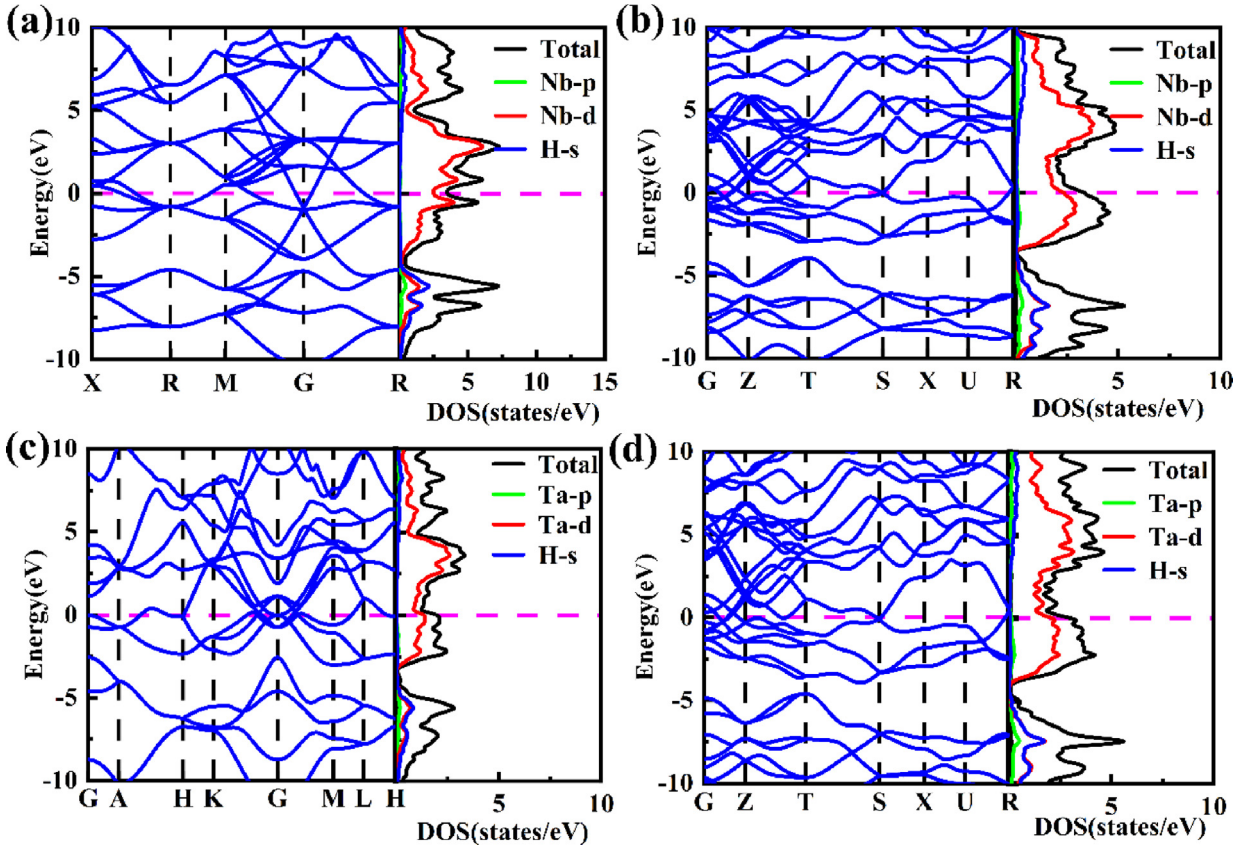

Fig. 3 The electronic band structure and densities of states (DOS) of (a) $Fm\bar{3}m$-NbH_2 at 1 atm, (b) *Pnma*-NbH_2 at 100 GPa, (c) $P6_3mc$-TaH_2 at 1 atm, and (d) *Pnma*-TaH_2 at 100 GPa.

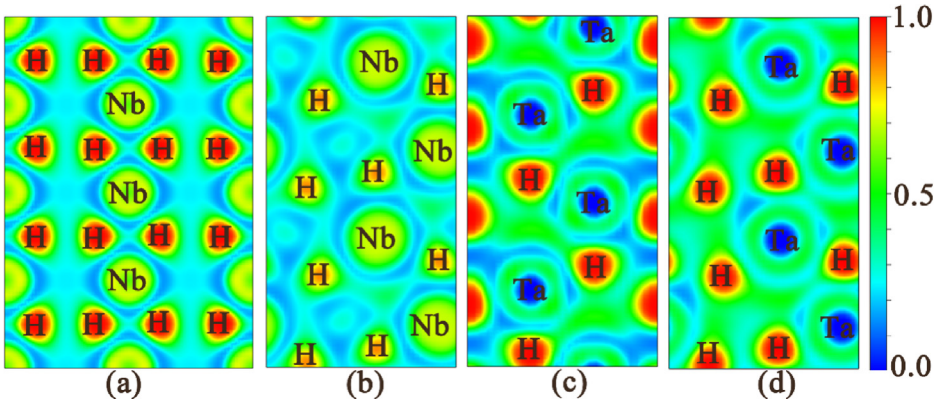

Fig. 4 Electron localization function (ELF) of for stable MH_2 (M = Nb, Ta) phases: (a) (−1 1 0) plane for the $Fm\bar{3}m$-NbH_2 phase at 1 atm, (b) (0 1 0) plane for the *Pnma*-NbH_2 phase at 100 GPa, (c) (1 1 0) plane for the $P6_3mc$-TaH_2 phase at 1 atm, and (d) (0 1 0) plane for the *Pnma*-TaH_2 phase at 100 GPa.

Table 3 Calculated Bader charges for NbH_2 and TaH_2 at the selected pressures. δ represents the amount of charge transferred from the mental atom to the H atom.

Phase	Space group	Pressure	Atom	Charge value (e)	δ (e)
NbH_2	$Fm\bar{3}m$	1 atm	Nb	11.70	1.30
			H	1.65	−0.65
	Pnma	100 GPa	Nb	11.98	1.02
			H	1.51	−0.51
TaH_2	$P6_3mc$	1 atm	Ta	9.82	1.18
			H	1.59	−0.59
	Pnma	100 GPa	Ta	9.96	1.04
			H	1.52	−0.52

atoms, demonstrating the ionic character of the M−H bonding in MH_2 (M = Nb, Ta) crystals. Such ionic bonding properties are similar in RhH_2 (Shao et al., 2021), ThH_2 (Zhang et al., 2015), TcH_2 (Li et al., 2016), TiH_2 (Zhuang et al., 2018), HfH_2 (Quijano et al., 2009), and VH_2 (Zhuang et al., 2017; Li and Peng, 2017), but differ from many hydrogen-rich polycrystalline forms (i.e. SiH_4 (Zhang et al., 2015), SnH_4 (Zhang et al., 2016), MgH_{12} (Lonie et al., 2013), MgH_{16} (Lonie et al., 2013), AsH_8 (Fu et al., 2016), RuH_6 (Liu et al., 2016); and MoH_{11} (Du et al., 2021) where H atoms are bonded to the nearest H atoms to form H_2 or H_3 units and/or they are covalently bonded to X (X = Si, Sn) to form X-H bonds. Combination analysis of ELF and Bader charges reveals that MH_2 (M = Nb, Ta) forms an ionic bond between M and H, and MH_2 (M = Nb, Ta) belongs to ionic crystal with the charge transfers from M atom to H atom, which is consistent with Poisson's ratio analysis mentioned above.

3.4. Electron–phonon coupling

For exploring the superconductivity, we calculate the logarithmic average phonon frequency ω_{log}, the electronic DOS at the Fermi level $N(E_f)$, and the EPC parameter λ as shown in Table 4. It is found that for materials with $\lambda < 1.5$, it is more accurate to estimate the superconducting temperature of the obtained structure by using the modified Allen-Dynes McMillan equation $T_c = \frac{\omega_{log}}{1.2} \exp\left[\frac{1.04(1+\lambda)}{\lambda-\mu^*(1+0.62\lambda)}\right]$ (Allen and Dynes, 1975). The estimated T_c of NbH_2 and TaH_2 with a typical choice of Coulomb pseudopotential μ^* = 0.1–0.13 is presented in Table 4, which shows that *Pnma*-NbH_2 has the highest T_c, and can reach 6.9 K at 50 GPa, higher than the maximal 4 K predicted for *Pnma*-VH_2 (Chen et al., 2014) at 60 GPa. The estimated T_c of $P6_3mc$-TaH_2 is 0.775–1.528 K at 1 atm, which is consistent with the experimental measurement of no superconducting transition in the temperature range of 4.4–300 K for TaH_2 (Kuzovnikov et al., 2017). In addition, the calculated T_c of the *Pnma*-TaH_2 is 3.586–5.542 K at 100 GPa, which is smaller than that of the *Pnma*-NbH_2 at 100 GPa. The main reason is that the electron DOS of *Pnma*-TaH_2 at Fermi level N (E_f) is much smaller than that of *Pnma*-NbH_2.

According to Fig. 5, we computed phonon dispersions, phonon density of states (PHDOS), Eliashberg spectral function ($\alpha^2F(\omega)/\omega$), and EPC integrated ($\lambda(\omega)$) for the $Fm\bar{3}m$-NbH_2 and $P6_3mc$-TaH_2 at 0 GPa, and the *Pnma*-NbH_2 and *Pnma*-TaH_2 at 100 GPa. As a result, we found that all structure is dynamically stable because it exhibits the absence of any imaginary frequencies (Zhang et al., 2022; Sun et al., 2020; Zheng et al., 2021; Li et al., 2022; Jin et al., 2022). A clear gap between acoustic and optical phonon modes is observed in the theoretical phonon density of states (Fig. 5), which is due to the huge difference in mass between the M (M = Nb, Ta) atom and H atom, thus dividing the phonon density of states into low-frequency vibrations of M (M = Nb, Ta) atom and high-frequency vibrations of H atom. Note that the low-frequency vibrational modes below 10 THz come from M

Table 4 The calculated logarithmic average phonon frequency ω_{log}, electronic density of states at the Fermi level $N(E_f)$ (states/spin/Ry/Unit cell), electron–phonon coupling parameters λ, and superconducting critical temperatures T_c of $Fm\bar{3}m$-NbH_2, *Pnma*-NbH_2, $P6_3mc$-TaH_2, and *Pnma*-TaH_2 at different pressures.

Phase	Structure	Pressure	ω_{log}(K)	$N(\varepsilon_f)$	λ	T_c(K)μ^* = 0.1	T_c(K)μ^* = 0.13
NbH_2	$Fm\bar{3}m$	1 atm	262.565	7.208	0.441	1.836	0.945
	Pnma	50 GPa	376.899	26.477	0.560	6.903	4.668
		100 GPa	394.013	20.208	0.550	6.795	4.485
		300 GPa	547.141	16.527	0.554	9.694	6.439
TaH_2	$P6_3mc$	1 atm	229.106	10.402	0.436	1.528	0.775
		50 GPa	297.577	7.146	0.325	0.299	0.071
	Pnma	100 GPa	348.496	16.927	0.537	5.542	3.586
		300 GPa	371.099	14.736	0.532	5.719	3.672

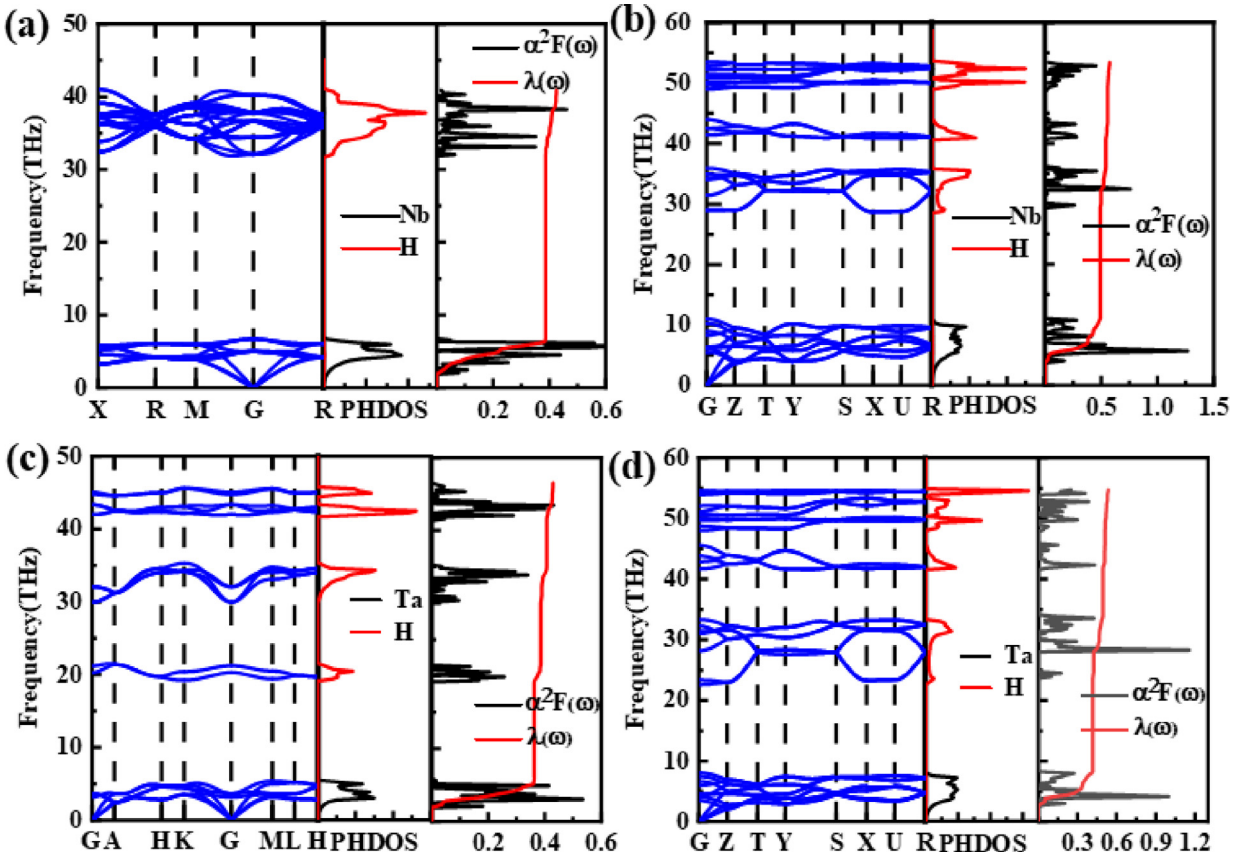

Fig. 5 Phonon dispersion relations, projected phonon densities of states (PHDOS), and Eliashberg spectral function for (a) $Fm\bar{3}m$-NbH_2 at 1 atm, (b) *Pnma*-NbH_2 at 100 GPa, (c) $P6_3mc$-TaH_2 at 1 atm, and (d) *Pnma*-TaH_2 at 100 GPa.

(M = Nb, Ta) atoms, accounting for 90.8 %, 85.5 %, 84.5 %, and 78 % of the total λ, respectively, while the high-frequency vibrational modes above 10 THz come from H atoms, accounting for 9.2 %, 14.5 %, 15.5 %, and 22 % of the total λ, respectively. We, therefore, conclude that the coupling between electron and phonon vibration of M (M = Nb, Ta) is the reason why MH_2 (M = Nb, Ta) shows superconductivity, which is consistent with the dominant DOS of M-*d* (M = Nb, Ta) shell at Fermi energy. For MH_2 (M = Nb, Ta), contrary to the case of superconducting H_3S (Drozdov et al., 2015; Duan et al., 2014), YH_3 (Kim et al., 2009), and PdH (Gupta, 1982), the electron-optical phonon contribution and consequently to T_c is small, due essentially to the low value of the DOS of H-*s* states at the Fermi energy, which leads to the low-T_c features of all MH_2 (M = Nb, Ta) phases.

3.5. *Pressure–temperature phase diagram*

As discussed earlier, we established a phase transition sequence of MH_2 (M = Nb, Ta) under pressure at 0 K. High pressure and high-temperature technology are very important for the synthesis of new materials. Here, the main function of pressure and temperature is to change the free energy diagram of materials or the reaction barrier between materials, so as to pro-

mote phase transition or chemical reaction, which leads to the formation and synthesis of the target phase, which can be stored in environmental conditions. To further discover the high-pressure synthesis conditions and the stable pressure–temperature region of each phase, the phase diagram of MH_2 (M = Nb, Ta) was constructed by using the quasi-harmonic approximation (QHA) method (Togo and Tanaka, 2015). At a given pressure and temperature, the Helmholtz free energy is expressed as:

$$F(V,T) = E(V) + F_{\mathrm{vib}}(V,T) + F_{el} \tag{2}$$

where E(V) is the cold static lattice energy with atoms being clamped at their equilibrium positions, F_{vib} (V, T) is the nonequilibrium vibrational Helmholtz free energy of phonons, and F_{el} is the electronic thermal excitation free energy. Of course, considering that the contribution of thermoelectrons (F_{el}) to free energy is negligible at relatively low temperatures, the F (V, T) we obtain does not include the contribution of electrons (Kvashnin et al., 2018; Yan et al., 2016; Rybkovskiy et al., 2020). F_{vib} (V, T) can be obtained from.

$$F_{\mathrm{vib}}(V,T) = \int_0^{\infty} \left[\frac{h\omega}{2} + \kappa_B T \ln\left(1 - e^{-h\omega/\kappa_B T}\right)\right] g(\omega, V) d\omega \tag{3}$$

where κ_{B} is Boltzmann's constant and g (ω, V) is the phonon density of state and depends on the crystal geometry. Then, the Gibbs free energy is given by.

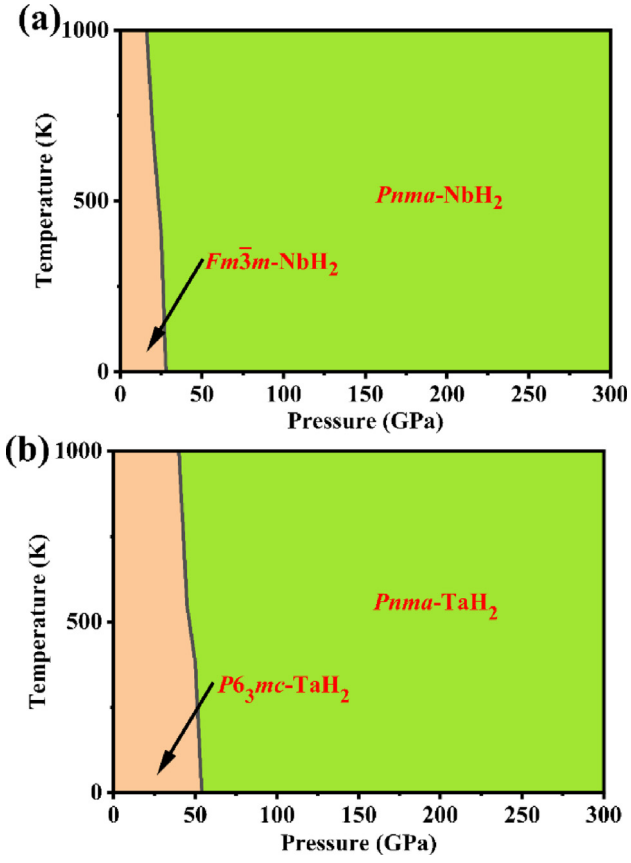

Fig. 6 Calculated temperature–pressure phase diagram of (a) NbH_2 and (b) TaH_2 based on quasi-harmonic approximation.

$$G_{\mathrm{gibbs}} = F(V,T) - V\left(\frac{\partial F}{\partial V}\right)_T \tag{4}$$

Therefore, based on the calculated Gibbs free energies of these phases at different temperatures and pressures, we obtain a pressure–temperature phase diagram (Fig. 6), which can determine the possible existence region of MH_2 (M = Nb, Ta) phases. According to Fig. 6, by comparing the transition pressures with and without the influence of temperature, we find that the transition pressure of NbH_2 from cubic $Fm\bar{3}m$ phase to orthorhombic *Pnma* phase at 0 K is 27.9 GPa, while the transition pressure of TaH_2 from the hexagonal $P6_3mc$ phase to orthorhombic *Pnma* phase at 0 K is 54.0 GPa. Therefore, ZPE does not change the phase transition series, but only reduces the phase transition pressure, especially for high-pressure transition, which is also observed in other hydrides, such as MgH_6 (Feng et al., 2015), AcH_2 (Jiang et al., 2014); and PtH (Gao et al., 2012). It is obvious that the transition pressures of $Fm\bar{3}m$-NbH_2 → *Pnma*-NbH_2 and $P6_3mc$-TaH_2 → *Pnma*-TaH_2 decrease obviously with the increase of temperature, which originates mainly from the contributions of the thermal vibration at the atomic position to the high-pressure structures more significantly than the low-pressure structures, thus significantly expanding their high-pressure structural stability fields.

4. Conclusions

In a word, we have extensively investigated the systematic structure evolution of MH_2 (M = Nb, Ta) compounds in the pressure range of 0 to 300 GPa by ab initio evolutionary simulation. Based on the structural prediction, the phase transition sequence of NbH_2 is $Fm\bar{3}m$ → *Pnma* at 48.8 GPa, while the TaH_2 is $P6_3mc$ → *Pnma* at 90.0 GPa, respectively. The calculations of elastic constants and phonon dispersions confirmed that these phases are stable. The analyses of DOS, Poisson's ratio, ELF, and Bader charge indicate that four MH_2 (M = Nb, Ta) phases are metallic and an ionic crystal with large amounts of charge transferring from M (M = Nb, Ta) atoms to H. The estimated superconducting transition temperature T_c values of *Pnma*-NbH_2 are 6.903 K at 50 GPa. In addition, it is found that the high-pressure phase transition of MH_2 (M = Nb, Ta) is more favorable upon heating, and this originates mainly from the contributions of the thermal vibration at the atomic position. The current research will stimulate further high-temperature and high-pressure experiments to synthesize these transition metal dihydrides and make structural, mechanical, and superconducting measurements.

Declaration of Competing Interest

The authors declare that they have no known competing financial interests or personal relationships that could have appeared to influence the work reported in this paper.

Acknowledgements

This work was supported by the National Natural Science Foundation of China (No. 11804031, 11904297 and 11747139), the Scientific Research Project of Education Department of Hubei Province (No. Q20191301) and Talent and High Level Thesis Development Fund of Department of Physics and Optoelectronic Engineering of Yangtze University (C. Z. Z.).

Appendix A. Supplementary material

Supplementary data to this article can be found online at https://doi.org/10.1016/j.arabjc.2022.104347.

References

Allen, P.B., Dynes, R.C., 1975. Transition temperature of strong-coupled superconductors reanalyzed. Phys. Rev. B 12, 905–922.

Becke, A.D., Edgecombe, K.E., 1990. A simple measure of electron localization in atomic and molecular systems. J. Chem. Phys. 92, 5397–5403.

Birch, F., 1947. Finite elastic strain of cubic crystals. Phys. Rev. 71, 809.

Bohnen, K.P., Heid, R., Renker, B., 2001. Phonon dispersion and electron-phonon coupling in MgB_2 and AlB_2. Phys. Rev. Lett. 86, 5771.

Chen, X.Q., Niu, H.Y., Li, D.Z., Li, Y.Y., 2011. Modeling hardness of polycrystalline materials and bulk metallic glasses. Intermetallics 19, 1275–1281.

Chen, W.H., Semenok, D.V., Huang, X.L., Shu, H., Li, X., Duan, D. F., Cui, T., Oganov, A.R., 2021. High-temperature superconducting phases in cerium superhydride with a T_c up to 115 K below a pressure of 1 megabar. Phys. Rev. Lett. 127, 117001.

Chen, C.B., Tian, F.B., Duan, D.F., Bao, K., Jin, X.L., Liu, B.B., Cui, T., 2014. Pressure induced phase transition in MH_2 (M = V, Nb). J. Chem. Phys. 140, 114703.

Choi, H.J., Roundy, D., Sun, H., Cohen, M.L., Louie, S., 2002. The origin of the anomalous superconducting properties of MgB_2. Nature 418, 758–760.

Drozdov, A.P., Eremets, M.I., Troyan, I.A., Ksenofontov, V., Shylin, S.I., 2015. Conventional superconductivity at 203 kelvin at high pressures in the sulfur hydride system. Nature 525, 73–76.

Drozdov, A.P., Kong, P.P., Minkov, V.S., Besedin, S.P., Kuzovnikov, M.A., Mozaffari, S., Balicas, L., Balakirev, F.F., Graf, D.E., Prakapenka, V.B., Greenberg, E., Knyazev, D.A., Tkacz, M., Eremets, M.I., 2019. Superconductivity at 250 K in lanthanum hydride under high pressures. Nature 569, 528–531.

Du, M.Y., Zhang, Z.H., Song, H., Yu, H.Y., Cui, T., Kresin, V.Z., Duan, D.F., 2021. High-temperature superconductivity in transition metallic hydrides MH_{11} (M = Mo, W, Nb, and Ta) under high pressure. PCCP 23, 6717–6724.

Duan, D., Liu, Y., Tian, F., Li, D., Huang, X., Zhao, Z., Yu, H., Liu, B., Tian, W., Cui, T., 2014. Pressure-induced metallization of dense $(H_2S)_2H_2$ with high-T_c superconductivity. Sci. Rep. 4, 1–6.

Errandonea, D., Ferrer-Roca, C., Martínez-Garcia, D., Segura, A., Gomis, O., Muñoz, A., Rodríguez-Hernández, P., López-Solano, L., Alconchel, S., Sapiña, F., 2010. High-pressure x-ray diffraction and ab initio study of Ni_2Mo_3N, Pd_2Mo_3N, Pt_2Mo_3N, Co_3Mo_3N, and Fe_3Mo_3N: Two families of ultra-incompressible bimetallic interstitial nitrides. Phys. Rev. B 82, 174105.

Feng, X.L., Zhang, J.R., Gao, G.Y., Liu, H.Y., Wang, H., 2015. Compressed sodalite-like MgH_6 as a potential high-temperature superconductor. RSC Adv. 5, 59292–59296.

Fu, Y.H., Du, X.P., Zhang, L.J., Peng, F., Zhang, M., Pickard, C.J., Needs, R.J., Singh, D.J., Zheng, W.T., Ma, Y.M., 2016. High-pressure phase stability and superconductivity of pnictogen hydrides and chemical trends for compressed hydrides. Chem. Mater. 28, 1746–1755.

Gao, G.Y., Wang, H., Zhu, L., Ma, Y.M., 2012. Pressure-induced formation of noble metal hydrides. J. Phys. Chem. C 116, 1995–2000.

Gao, G.Y., Bergara, A., Liu, G.T., Ma, Y.M., 2013. Pressure induced phase transitions in TiH_2. J. Appl. Phys. 113, 103512.

Gao, G.Y., Hoffmann, R., Ashcroft, N.W., Liu, H.Y., Bergara, A., Ma, Y.M., 2013. Theoretical study of the ground-state structures and properties of niobium hydrides under pressure. Phys. Rev. B 88, 184104.

Giannozzi, P., Baroni, S., Bonini, N., Calandra, M., Car, R., Cavazzoni, C., Ceresoli, D., Chiarotti, G.L., Cococcioni, M., Dabo, I., Dal Corso, A., de Gironcoli, S., Fabris, S., Fratesi, G., Gebauer, R., Gerstmann, U., Gougoussis, C., Kokalj, A., Lazzeri, M., Martin-Samos, L., Marzari, N., Mauri, F., Mazzarello, R., Paolini, S., Pasquarello, A., Paulatto, L., Sbraccia, C., Scandolo, S., Sclauzero, G., Seitsonen, A.P., Smogunov, A., Umari, P., Wentzcovitch, R.M., 2009. QUANTUM ESPRESSO: a modular and open-source software project for quantum simulations of materials. J. Phys.: Condens. Matter 21, 395502.

Gupta, M., 1982. Electronic properties and electron-phonon coupling in zirconium and niobium hydrides. Phys. Rev. B 25, 1027.

Haines, J., Leger, J., Bocquillon, G., 2001. Synthesis and design of superhard materials. Annu. Rev. Mater. Sci. 31, 1.

Hill, R., 1952. The elastic behaviour of a crystalline aggregate. Proc. Phys. Soc. London, Sect. A 65, 349.

Hong, F., Shan, P.F., Yang, L.X., Yue, B.B., Yang, P.T., Liu, Z.Y., Sun, J.P., Dai, J.H., Yu, H., Yin, Y.Y., Yu, X.H., Cheng, J.G., Zhao, Z.X., 2021. Superconductivity at 70 K in tin hydride SnHx under high pressure. arXiv preprint arXiv:2101.02846.

Huang, X.L., Duan, D.F., Li, F.F., Huang, Y.P., Wang, L., Liu, Y.X., Bao, K., Zhou, Q., Liu, B.B., Cui, T., 2014. Structural stability and compressive behavior of ZrH_2 under hydrostatic pressure and nonhydrostatic pressure. RSC Adv. 4, 46780–46786.

Jiang, H., Wang, W., Zhang, C., Hu, X.N., Zhong, G.H., Lu, X.Q., Su, Y.H., 2014. Phase transitions of actinium dihydride: Pressure-induced charge transfer driving effect. Int. J. Hydrog. Energy 39, 15827–15835.

Jin, Y.Y., Zhang, J.Q., Ling, S., Wang, Y.Q., Li, S., Kuang, F.G., Wu, Z.Y., Zhang, C.Z., 2022. Pressure-induced novel structure with graphene-like boron-layer in titanium monoboride. Chin. Phys. B. https://doi.org/10.1088/1674-1056/ac9222.

Junkaew, A., Ham, B., Zhang, X., Arróyave, R., 2014. Ab-initio calculations of the elastic and finite-temperature thermodynamic properties of niobium-and magnesium hydrides. Int. J. Hydrog. Energy 39, 15530–15539.

Kalita, P.E., Sinogeikin, S.V., Lipinska-Kalita, K., Hartmann, T., Ke, X.Z., Chen, C.F., Cornelius, A., 2010. Equation of state of TiH_2 up to 90 GPa: A synchrotron x-ray diffraction study and ab initio calculations. J. Appl. Phys. 108, 043511.

Kanagaprabha, S., Asvinimeenaatci, A.T., Sudhapriyanga, G., Jemmy Cinthia, A., Rajeswarapalanichamy, R., Iyakutti, K., 2013. First principles study of stability and electronic structure of TMH and TMH_2 (TM = Y, Zr, Nb). Acta Phys. Pol. 123, 126–131.

Kim, D.Y., Scheicher, R.H., Ahuja, R., 2009. Predicted high-temperature superconducting state in the hydrogen-dense transition-metal hydride YH_3 at 40 K and 17.7 GPa. Phys. Rev. Lett. 103, 077002.

Kim, D.Y., Scheicher, R.H., Pickard, C.J., Needs, R.J., Ahuja, R., 2011. Predicted formation of superconducting platinum-hydride crystals under pressure in the presence of molecular hydrogen. Phys. Rev. Lett. 107, 117002.

Kong, P.P., Minkov, V.S., Kuzovnikov, M.A., Drozdov, A.P., Besedin, S.P., Mozaffari, S., Balicas, L., Balakirev, F.F., Prakapenka, V.B., Chariton, S., Knyazev, D.A., Greenberg, E., Eremets, M.I., 2021. Superconductivity up to 243 K in the yttrium-hydrogen system under high pressure. Nat. Commun. 12, 1–9.

Kresse, G., Furthmüller, J., 1996. Efficient iterative schemes for ab initio total-energy calculations using a plane-wave basis set. Phys. Rev. B 54, 11169.

Kresse, G., Joubert, D., 1999. From ultrasoft pseudopotentials to the projector augmented-wave method. Phys. Rev. B 59, 1758.

Kruglov, I.A., Kvashnin, A.G., Goncharov, A.F., Oganov, A.R., Lobanov, S.S., Holtgrewe, N., Jiang, S., Prakapenka, V.B., Greenberg, E., Yanilkin, A.V., 2018. Uranium polyhydrides at moderate pressures: Prediction, synthesis, and expected superconductivity. Sci. Adv. 4, eaat9776.

Kuzovnikov, M.A., Tkacz, M., Meng, H.J., Kapustin, D.I., Kulakov, V.I., 2017. High-pressure synthesis of tantalum dihydride. Phys. Rev. B 96, 134120.

Kuzovnikov, M.A., Antonov, V.E., Ivanov, A.S., Hansen, T., Savvin, S., Kulakov, V.I., Tkacz, M., Kolesnikov, A.I., Gurev, V.M., 2020. Neutron scattering study of tantalum dihydride. Phys. Rev. B 102, 024113.

Kvashnin, A.G., Zakaryan, H.A., Zhao, C., Duan, Y., Kvashnina, Y. A., Xie, C., Oganov, A.R., 2018. New tungsten borides, their stability and outstanding mechanical properties. J. Phys. Chem. Lett. 9, 3470–3477.

Li, B., Ding, Y., Kim, D.Y., Ahuja, R., Zou, G.T., Mao, H.K., 2011. Rhodium dihydride (RhH_2) with high volumetric hydrogen density. PNAS 108, 18618–18621.

Li, Z.W., He, X., Zhang, C.L., Wang, X.C., Zhang, S.J., Jia, Y.T., Feng, S.M., Lu, K., Zhao, J.F., Zhang, J., Min, B.S., Long, Y.W., Yu, R.C., Wang, L.H., Ye, M.Y., Zhang, Z.S., Prakapenka, V., Chariton, S., Ginsberg, P.A., Bass, J., Yuan, S.H., Liu, H.Z., Jin, C.Q., 2022. Superconductivity above 200 K discovered in superhydrides of calcium. Nat. Commun. 13, 1–5.

Li, X.F., Liu, H.Y., Peng, F., 2016. Crystal structures and superconductivity of technetium hydrides under pressure. PCCP 18, 28791–28796.

Li, X., Peng, F., 2017. Superconductivity of pressure-stabilized vanadium hydrides. Inorg. Chem. 56, 13759–13765.

Li, X., Huang, X.L., Duan, D.F., Pickard, C.J., Zhou, D., Xie, H., Zhuang, Q., Huang, Y.P., Zhou, Q., Liu, B.B., Cui, T., 2019. Polyhydride CeH_9 with an atomic-like hydrogen clathrate structure. Nat. Commun. 10, 1–7.

Li, S., Wang, H., Sun, W., Lu, C., Peng, F., 2022. Superconductivity in compressed ternary alkaline boron hydrides. Phys. Rev. B 105, 224107.

Liu, G.T., Besedin, S., Irodova, A., Liu, H.Y., Gao, G.Y., Eremets, M., Wang, X., Ma, Y.M., 2017. Nb-H system at high pressures and temperatures. Phys. Rev. B 95, 104110.

Liu, Y.X., Huang, X.L., Duan, D.F., Tian, F.B., Liu, H.Y., Li, D., Zhao, Z.L., Sha, X.J., Yu, H.Y., Zhang, H.D., Liu, B.B., Cui, T., 2015. First-principles study on the structural and electronic properties of metallic HfH_2 under pressure. Sci. Rep. 5, 11381.

Liu, Y.X., Duan, D.F., Tian, F.B., Wang, C., Ma, Y.B., Li, D., Huang, X.L., Liu, B.B., Cui, T., 2016. Stability and properties of the Ru−H system at high pressure. PCCP 18, 1516–1520.

Lonie, D.C., Hooper, J., Altintas, B., Zurek, E., 2013. Metallization of magnesium polyhydrides under pressure. Phys. Rev. B 87, 054107.

Lyakhov, A.O., Oganov, A.R., Stokes, H.T., Zhu, Q., 2013. New developments in evolutionary structure prediction algorithm USPEX. Comput. Phys. Commun. 184, 1172–1182.

Ma, L., Wang, K., Xie, Y., Yang, X., Wang, Y.Y., Zhou, M., Liu, H. Y., Yu, X.H., Zhao, Y.S., Wang, H.B., Liu, G.T., Ma, Y.M., 2022. High-temperature superconducting phase in clathrate calcium hydride CaH_6 up to 215 K at a pressure of 172 GPa. Phys. Rev. Lett. 128, 167001.

Miao, M.S., Sun, Y.H., Zurek, E., Lin, H.Q., 2020. Chemistry under high pressure. Nat. Rev. Chem. 4, 508–527.

Miwa, K., Fukumoto, A., 2002. First-principles study on 3d transition-metal dihydrides. Phys. Rev. B 65, 155114.

Monkhorst, H.J., Pack, J.D., 1976. Special points for Brillouin-zone integrations. Phys. Rev. B 13, 5188.

Oganov, A.R., Glass, C.W., 2006. Crystal structure prediction using ab initio evolutionary techniques: principles and applications. J. Chem. Phys. 124, 244704.

Oganov, A.R., Lyakhov, A.O., Valle, M., 2011. How evolutionary crystal structure prediction works−and why. Acc. Chem. Res. 44, 227–237.

Pan, Y., Chen, S., 2020. Exploring the novel structure, transportable capacity and thermodynamic properties of TiH_2 hydrogen storage material. Int. J. Energy Res. 44, 4997–5007.

Perdew, J.P., Burke, K., Ernzerhof, M., 1996. Generalized gradient approximation made simple. Phys. Rev. Lett. 77, 3865.

Pickard, C.J., Needs, R.J., 2007. Structure of phase III of solid hydrogen. Nat. Phys. 3, 473–476.

Pugh, S., 1954. Xcii. relations between the elastic moduli and the plastic properties of polycrystalline pure metals. Phil. Mag. 45, 823–843.

Purans, J., Menushenkov, A., Besedin, S., Ivanov, A., Minkov, V., Pudza, I., Kuzmin, A., Klementiev, K., Pascarelli, S., Mathon, O., Rosa, A.D., Irifune, T., Eremets, M.I., 2021. Local electronic structure rearrangements and strong anharmonicity in YH_3 under pressures up to 180 GPa. Nat. Commun. 12, 1–10.

Quijano, R., de Coss, R., Singh, D.J., 2009. Electronic structure and energetics of the tetragonal distortion for TiH_2, ZrH_2, and HfH_2: A first-principles study. Phys. Rev. B 80, 184103.

Rahman, S., Saqib, H., Liang, X., Errandonea, D., Resta, A.S., Molina-Sanchez, A., Gao, G., Wang, L., Tian, Y., Mao, H.K., 2022. Pressure-induced metallization and robust superconductivity in pristine 1T-$HfSe_2$. Mater. Today Phys. 25, 100698.

Reilly, J.J., Wiswall, R.H., 1970. Higher hydrides of vanadium and niobium. Inorg. Chem. 9, 1678–1682.

Rybkovskiy, D.V., Kvashnin, A.G., Kvashnina, Y.A., Oganov, A.R., 2020. Structure, stability, and mechanical properties of boron-rich Mo–B phases: a computational study. J. Phys. Chem. Lett. 11, 2393–2401.

Saitoh, H., Takagi, S., Sato, T., Orimo, S.i., 2021. Pressure temperature phase diagram of Ta-H system up to 9 GPa and 600 ℃. Appl. Sci. 11, 6719.

Salke, N.P., Esfahani, M.M.D., Zhang, Y.J., Kruglov, I.A., Zhou, J. S., Wang, Y.G., Eran Greenberg, V.B.P., Liu, J., Oganov, A.R., Lin, J.F., 2019. Synthesis of clathrate cerium superhydride CeH_9 at 80–100 GPa with atomic hydrogen sublattice. Nat. Commun. 10, 1–10.

Saqib, H., Rahman, S., Zhao, Y., Cazorla, C., Errandonea, D., Susilo, R., Zhuang, Y., Huang, Y., Chen, B., Dai, N., 2021. Evolution of structural and electronic properties of $TiSe_2$ under high pressure. J. Phys. Chem. Lett. 12, 9859–9867.

Savin, A., Jepsen, O., Flad, J., Andersen, O.K., Preuss, H., von Schnering, H.G., 1992. Electron localization in solid-state structures of the elements: the diamond structure. Angew. Chem. Int. Ed. 31, 187–188.

Scheler, T., Marqués, M., KonÔpkoá, Z., Guillaume, C.L., Howie, R. T., Gregoryanz, E., 2013. High-pressure synthesis and characterization of iridium trihydride. Phys. Rev. Lett. 111, 215503.

Semenok, D.V., Kvashnin, A.G., Ivanova, A.G., Svitlyk, V., Fominski, V.Y., Sadakov, A.V., Sobolevskiy, O.A., Pudalov, V.M., Troyan, I.A., Oganov, A.R., 2020. Superconductivity at 161 K in thorium hydride ThH_{10}: Synthesis and properties. Mater. Today 33, 36–44.

Shao, Z.J., Duan, D.F., Wang, L.Y., Song, H., Yu, H.Y., Yao, Y.S., Cui, T., 2021. First-principles investigation of rhodium hydrides under high pressure. Phys. Rev. B 104, 054110.

Smithson, H., Marianetti, C.A., Morgan, D., Van der Ven, A., Predith, A., Ceder, G., 2002. First-principles study of the stability and electronic structure of metal hydrides. Phys. Rev. B 66, 144107.

Snider, E., Dasenbrock-Gammon, N., McBride, R., Wang, X.Y., Meyers, N., Lawler, K.V., Zurek, E., Salamat, A., Dias, R.P., 2021. Synthesis of yttrium superhydride superconductor with a transition temperature up to 262 K by catalytic hydrogenation at high pressures. Phys. Rev. Lett. 126, 117003.

Sun, W., Kuang, X., Keen, H.D., Lu, C., Hermann, A., 2020. Second group of high-pressure high-temperature lanthanide polyhydride superconductors. Phys. Rev. B 102, 144524.

Talantsev, E.F., 2021. Comparison of highly-compressed $C2/m$-SnH_{12} superhydride with conventional superconductors. J. Phys.: Condens. Matter 33, 285601.

Tang, W., Sanville, E., Henkelman, G., 2009. A grid-based bader analysis algorithm without lattice bias. J. Phys.: Condens. Matter 21, 084204.

Togo, A., Oba, F., Tanaka, I., 2008. First-principles calculations of the ferroelastic transition between rutile-type and $CaCl_2$-type SiO_2 at high pressures. Phys. Rev. B 78, 134106.

Togo, A., Tanaka, I., 2015. First principles phonon calculations in materials science. Scr. Mater. 108, 1–5.

Troyan, I.A., Semenok, D.V., Kvashnin, A.G., Sadakov, A.V., Sobolevskiy, O.A., Pudalov, V.M., Ivanova, A.G., Prakapenka, V.B., Eran Greenberg, A.G.G., Lyubutin, I.S., Struzhkin, V.V., Bergara, A., Errea, I., Bianco, R., Calandra, M., Mauri, F., Monacelli, L., Akashi, R., Oganov, A.R., 2021. Anomalous high-temperature superconductivity in YH_6. Adv. Mater. 33, 2006832.

Wang, W.J., Zhang, C.Z., Jin, Y.Y., Li, S., Zhang, W.B., Kong, P.L., Xie, C.W., Du, C.Z., Liu, Q., Zhang, C.H., 2020. Structural, mechanical and electronic properties and hardness of ionic vanadium dihydrides under pressure from first-principles computations. Sci. Rep. 10, 8868.

Wei, Y.K., Yuan, J.N., Khan, F.I., Ji, G.F., Gu, Z.W., Wei, D.Q., 2016. Pressure induced superconductivity and electronic structure properties of scandium hydrides using first principles calculations. RSC Adv. 6, 81534–81541.

Yan, X., Chen, Y., Xiang, S., Kuang, X., Bi, Y., Chen, H., 2016. High-temperature-and high-pressure-induced formation of the Laves-phase compound XeS_2. Phys. Rev. B 93, 214112.

Ye, X.Q., Hoffmann, R., Ashcroft, N.W., 2015. Theoretical study of phase separation of scandium hydrides under high pressure. J. Phys. Chem. C 119, 5614–5625.

Ying, J.J., Li, X., Greenberg, E., Prakapenka, V.B., Liu, H.Y., Struzhkin, V.V., 2019. Synthesis and stability of tantalum hydride at high pressures. Phys. Rev. B 99, 224504.

Zhang, C., Guo, S.P., Jiang, H., Zhong, G.H., Su, Y.H., 2015. Zero-point effects on phase transitions of thorium dihydride under high pressure. J. Phys. Chem. C 119, 13465–13471.

Zhang, H.D., Jin, X.L., Lv, Y.Z., Zhuang, Q., Liu, Y.X., Lv, Q.Q., Bao, K., Li, D., Liu, B.B., Cui, T., 2015. High-temperature superconductivity in compressed solid silane. Sci. Rep. 5, 8845.

Zhang, H.D., Jin, X.L., Lv, Y.Z., Zhuang, Q., Li, Y., Bao, K., Li, D., Liu, B.B., Cui, T., 2016. Pressure-induced phase transition of SnH_4: a new layered structure. RSC Adv. 6, 10456–10461.

Zhang, J.Q., Jin, Y.Y., Zhang, C.Z., Wang, Y.Q., Tang, L.B., Li, S., Ju, M., Wang, J.J., Sun, W.G., Dou, X.L., 2022. The crystal structures, phase stabilities, electronic structures and bonding features of iridium borides from first-principles calculations. RSC Adv. 12, 11722–11731.

Zhang, C.Z., Sun, G.L., Wang, J.J., Lu, C., Jin, Y.Y., Kuang, X.Y., Hermann, A., 2017. Prediction of novel high-pressure structures of magnesium niobium dihydride. ACS Appl. Mater. Interfaces 9, 26169–26176.

Zheng, J., Sun, W., Dou, X., Mao, A.J., Lu, C., 2021. Pressure-driven structural phase transitions and superconductivity of ternary hydride $MgVH_6$. J. Phys. Chem. C 125, 3150–3156.

Zhuang, Q., Jin, X.L., Cui, T., Ma, Y.B., Lv, Q.Q., Li, Y., Zhang, H. D., Meng, X., Bao, K., 2017. Pressure-stabilized superconductive ionic tantalum hydrides. Inorg. Chem. 56, 3901–3908.

Zhuang, Q., Jin, X.L., Lv, Q.Q., Li, Y., Shao, Z.J., Liu, Z., Li, X., Zhang, H.D., Meng, X., Bao, K., Cui, T., 2017. Investigation of superconductivity in compressed vanadium hydrides. PCCP 19, 26280–26284.

Zhuang, Q., Jin, X.L., Cui, T., Zhang, D., Li, Y., Li, X., Bao, K., Liu, B.B., 2018. Effect of electrons scattered by optical phonons on superconductivity in MH_3(M = S, Ti, V, Se). Phys. Rev. B 98, 024514.